

GaAs/InGaAs/AlGaAs HETEROSTRUCTURE BARRIER VARACTORS FOR FREQUENCY TRIPLING

J. R. Jones, S. H. Jones, and G. B. Tait[†]

Department of Electrical Engineering, University of Virginia, Charlottesville, VA 22903

[†]Electronics Science & Technology Division, Naval Research Laboratory, Washington, DC 20375

Abstract

Accurate and efficient calculations of the large-signal time-dependent behavior of GaAs/InGaAs/AlGaAs Heterostructure Barrier Varactor (HBV) frequency tripler circuits are presented. This is accomplished by combining a novel harmonic-balance nonlinear circuit analysis technique with a hydrodynamic device simulator based on the first two moments of the Boltzmann transport equation and Poisson's equation. The unified numerical device/harmonic-balance nonlinear circuit simulator allows HBV multiplier circuits to be co-designed from both a device and a circuit point of view by specifying the device geometry, doping profile, and alloy composition profile, as well as the parasitic impedances of the device and the embedding impedances of the circuit. Excellent correlation between the numerical device simulator and experimental DC I-V and static C-V data has been obtained for GaAs/AlGaAs, GaAs/InGaAs/AlGaAs, and InGaAs/InAlAs on InP HBVs. Harmonic-balance simulations of GaAs/Al_{0.7}Ga_{0.3}As and GaAs/In_{0.0-0.2}Ga_{1.0-0.8}As/Al_{0.7}Ga_{0.3}As HBVs indicate that an improvement in tripler performance can be achieved using the GaAs/graded InGaAs/AlGaAs structure. Third harmonic output power levels of several milliwatts and multiplying efficiencies of at least 7.0 % are obtainable from these two device structures, for frequency tripling from 100 GHz to 300 GHz, with nominal parasitic device impedances and realizable fundamental and third harmonic circuit embedding impedances.

I. Introduction

The Heterostructure Barrier Varactor (HBV), first proposed in 1989[1], has received considerable attention as a promising device for high efficiency frequency multiplication in the millimeter to submillimeter wavelength range because of its attractive device characteristics and large number of design parameters. A single barrier HBV consists of a large band gap semiconductor sandwiched between symmetric capacitive modulation regions of smaller band gap material such that the device has an evenly symmetric nonlinear capacitance-voltage (C-V) relationship at zero DC bias. The evenly symmetric device C-V characteristic eliminates the even harmonic components from the output current waveform so that high efficiency frequency multiplier circuits, which do not require DC bias and which require fewer idlers than standard Schottky varactor multipliers,

can be realized. These device characteristics make the HBV an ideal candidate for use in broadband frequency triplers and quasi-optical tripler arrays, especially since no idlers are required for frequency tripling. By epitaxially stacking several single barrier HBVs in series, further advantages are expected including higher device cut-off frequencies, for a given device area, due to reduced device capacitances, and higher power generation capabilities due to the distribution of pump power over several series devices. Furthermore, the HBV has a large degree of design flexibility in that the semiconductor alloy composition and doping profiles, barrier thickness, number of barriers, device geometry, and device area can be independently varied. Overall, the design flexibility and attractive device characteristics of the HBV suggest that a high efficiency frequency multiplier with excellent device/circuit impedance matching and near-optimum C-V relationship can be achieved with a single device.

The large number of device design parameters coupled with the circuit design constraints makes the task of designing HBV frequency multipliers a daunting one. With this in mind, a DC and large-signal time-dependent numerical device simulator, with excellent computational speed and convergence properties, has been developed for generic InGaAs/InAlAs on InP and GaAs/InGaAs/AlGaAs HBVs. The simulator is based on the first two moments of the Boltzmann transport equation and combines electron transport through the heterostructure bulk with electron transport across the abrupt heterointerfaces in a fully self-consistent manner. The simulator can model any combination of doping and InGaAs, AlGaAs, or InAlAs alloy composition profiles such that a systematic investigation of candidate HBV devices can be undertaken to illuminate the combination of device geometry, doping profile, and alloy composition profile which yields optimal device performance. Given the importance of both the nonlinear device and its embedding circuit in the design of frequency multipliers, the numerical device simulator has been combined with a efficient harmonic-balance nonlinear circuit analysis technique to provide a unified computer-aided design environment for the entire HBV multiplier circuit. HBV multiplier circuits can, therefore, be co-designed from both a device and a circuit point of view by specifying the device geometry, doping profile, and alloy composition profile, as well as the

parasitic impedances of the device and the embedding impedances of the circuit.

An overview of the DC and large-signal time-dependent numerical device simulator is given in Section II. Likewise, a brief overview of the harmonic-balance nonlinear circuit analysis technique utilized in this work is presented in Section III. Experimental and theoretical DC, large-signal time-dependent, and harmonic-balance results are discussed in Section IV. Finally, conclusions are given in Section V.

II. Numerical Device Simulator

Given the essentially one-dimensional geometry of the HBV and the majority carrier nature of HBV operation, carrier transport through the bulk regions of an HBV has been described by a set of coupled nonlinear differential equations for electrons derived from the first two moments of the Boltzmann transport equation and Poisson's equation. These equations are valid in regions with smoothly varying alloy composition, and hydrodynamically model the scattering and diffusive transport mechanisms of electrons within the device. The resulting equations governing DC and large-signal time-dependent transport are

$$\frac{\partial J_{n,p}(x,t)}{\partial x} = \frac{1}{q} \frac{\partial n(x,t)}{\partial t} \quad (1)$$

$$J_{n,p}(x,t) = -\tau_p(x) \frac{\partial J_{n,p}(x,t)}{\partial t} - \frac{q^2 \tau_p(x) n(x,t)}{m^*(x)} \frac{\partial \phi_n(x,t)}{\partial x} \quad (2)$$

$$\frac{\partial}{\partial x} \left[\epsilon(x) \frac{\partial \psi(x,t)}{\partial x} \right] = q [n(x,t) - N_D(x)] \quad (3)$$

where

$$n(x,t) = n_{i,ref} \exp \left[\frac{q}{kT} (\psi(x,t) + V_n(x) - \phi_n(x,t)) \right] \quad (4)$$

and where $J_{n,p}$ is the electron particle current density, n is the electron density, ϕ_n is the electron quasi-Fermi potential, ψ is the electrostatic potential, k is Boltzmann's constant, q is the electron charge, T is the absolute temperature, $n_{i,ref}$ is the intrinsic electron density in

the reference material (GaAs or InP), and τ_p , m^* , and ϵ are the spatially-dependent momentum relaxation time, electron conductivity effective mass, and dielectric permittivity, respectively. Furthermore, V_n is the spatially-dependent alloy potential, referenced to intrinsic GaAs or InP, which models the additional electric force, caused by gradients in the electron affinity and the effective conduction band density of states, that electrons are subjected to in compositionally nonuniform materials[2]. In all, equation (1) is the electron current continuity equation and equation (3) is Poisson's equation. Equation (2) is the electron particle current density expression derived from the first moment of the Boltzmann equation, and includes the time-dependent term not included in the standard drift-diffusion equations. This extra term has been retained to help model ballistic transport phenomenon in the thin barrier region of the HBV, and high frequency transport phenomenon throughout the device.

In order to accurately model the current in heterostructure devices, it has been found that careful consideration of carrier transport across abrupt material discontinuities is required[3,4]. As such, electron transport across the abrupt heterointerfaces of an HBV has been described by a set of nonlinear electron particle current density equations which couple together the quasi-Fermi potentials on both sides of the interfaces and act as constraints on the particle current density throughout the device. Electric displacement continuity, electrostatic potential continuity, and electron particle current density continuity complete the set of interface conditions required for a self-consistent solution at a given heterointerface.

For an HBV biased as shown in Figure 1, the particle current density constraint at $x = 0$ takes into account thermionic emission and thermionic-field emission (thermally assisted tunneling) of carriers over and through the abrupt barrier, and is derived from an evaluation of the net flux of carriers crossing the heterointerface as given by emission theory and assuming a Maxwell-Boltzmann electron distribution[4]. The resulting interface constraint on the electron particle current at this junction is

$$J_{n,p}(0) = \frac{A^* T^2}{N_c(0^*)} \left\{ \exp \left[\frac{q}{kT} (\phi_n(0^+) - \phi_n(0^-)) \right] - 1 \right\} \left\{ n_{i,ref} \exp \left[\frac{q}{kT} \left(\frac{\Phi}{q} + \psi(0) + V_n(0^+) - \phi_n(0^+) \right) \right] \right\} \quad (5)$$

where A^* is the effective Richardson constant, Φ is the effective barrier height lowering due to tunneling, and the last term in braces in equation (5) is the electron density on the barrier side of the junction, $n(0^+)$.

At the $x = W$ heterointerface of Figure 1, the thermionic emission/thermionic-field emission electron particle current density constraint of equation (5) becomes a “fluid-outflow” constraint on electron transport. Under such high field conditions, the particle current density constraint is, again, derived from an evaluation of the net flux of carriers crossing the heterointerface as given by emission theory, but a full drifted-Maxwellian electron distribution is utilized instead of a Maxwell-Boltzmann distribution. The resulting interface constraints on the electron particle current at this junction is

$$J_{n,p}(W) = \{ \langle v_x \rangle_{R \rightarrow L} \exp[\phi_n(W^-) - \phi_n(W^+)] - \langle v_x \rangle_{L \rightarrow R} \} \{ n_{i,ref} \exp[\psi(W) + V_n(W^-) - \phi_n(W^-)] \} \quad (6)$$

where the first term in braces in equation (6) is interpreted as an average interface collection velocity and the last term in braces in this equation is the electron density on the barrier side of the junction, $n(W^-)$. The left and right directed components of the average interface collection velocity are given by, respectively

$$\langle v_x \rangle_{R \rightarrow L} = \sqrt{\frac{kT}{2\pi m_{D-M}^*}} \quad (7)$$

$$\langle v_x \rangle_{L \rightarrow R} = \sqrt{\frac{kT}{2\pi m_{D-M}^*}} \exp\left[\frac{-h^2 k_o^2}{8\pi k T m_{D-M}^*}\right] + \frac{hk_o}{4\pi m_{D-M}^*} \left\{ 1 + \operatorname{erf}\left[\frac{hk_o}{2\pi\sqrt{2kTm_{D-M}^*}}\right] \right\} \quad (8)$$

where

$$k_o = \frac{-J_{n,p}(W)}{n(W^-)} \quad (9)$$

is the displacement of the Maxwellian distribution from equilibrium and m_{D-M}^* is a suitable average of electron effective masses on the two sides of the heterointerface. In all, the interface constraint given by equation (6) is similar to the boundary constraint of Adams and Tang for Schottky contacts at high forward bias when the flat-band condition is exceeded[5].

Electrons can tunnel through the tip of the heterojunction barrier under appropriate bias conditions, i.e. at the $x = 0$ heterointerface in Figure 1. Since this tip closely resembles a triangular barrier, the WKB approximation for tunneling through the tip of a triangular barrier has been used to estimate the contribution of tunneling electrons to the total electron particle current as given in equation (5). By using the WKB approximation, the barrier height is, in effect, reduced by an amount[6]

$$\Phi = \frac{-3h\xi \ln(P)}{8\pi\sqrt{2qm_B^*}} \quad (10)$$

where h is Plank's constant, ξ is the total electric field in the barrier, m_B^* is the electron effective mass in the barrier, and P is the tunneling probability, or the probability of the triangular barrier being penetrated by an electron with energy Φ less than the height of the barrier. The electric field dependency of Φ is self-consistently determined during the numerical simulations.

The carrier transport equations are solved in two steps. First, the thermal equilibrium values of the state variables are obtained from the discretized nonlinear Poisson equation using a globally convergent nonlinear iterative technique[7]. The carrier transport equations are then solved at a given bias value via the coupled equation Newton-Raphson method. For the initial bias value, the thermal equilibrium solution serves as the starting point for the method; for subsequent bias values, the previous solution serves as the starting point. This procedure is very important since good initial conditions are required for convergence of the Newton method, and initial conditions derived from analytical approximations are not available for complex heterostructures. In our implementation of the Newton method, an exact Jacobian operator is formulated from the continuous system of coupled nonlinear transport equations. The resulting linearized system of equations is then discretized using a trapezoidal rule finite-difference scheme over a nonuniform mesh and solved by LU decomposition. In order to enhance the convergence range of the method, the Newton correction vectors are damped.

The transport equations are subject to constraints at both the device domain boundaries and the heterointerfaces. In order to utilize existing numerical codes which

solve two-point boundary value problems, all of the constraints are mapped onto two boundary points by appropriately “folding/translating” portions of the device domain and rescaling the transport equations in these regions. For a single barrier HBV, this means “folding,” at the heterointerfaces, the barrier region back onto the first modulation region, and “translating” the second modulation region onto the first modulation region. Unfortunately, this technique triples the number of equations to be solved since solution of the transport equations is now required in three regions (one barrier and two modulation) of the device. In addition, careful mesh construction is required since the mesh of the first modulation region is imposed on the barrier and second modulation regions.

In order to develop a robust numerical device simulator which could be efficiently combined with a harmonic-balance nonlinear circuit simulator, careful consideration was given to developing a DC and large-signal time-dependent device simulator with excellent numerical convergence and accuracy properties. Potential problems and inefficiencies were minimized by, among others, the following considerations:

- 1) The electron quasi-Fermi potential is chosen as a state variable instead of the electron density. This provides improved scaling of the Jacobian matrix and, since the magnitudes of potentials do not change by more than an order of magnitude across the entire mesh, superior accuracy control is obtained. In addition, very small currents, down to zero current, can be accurately resolved when the electron particle current density equation is formulated using the electron quasi-Fermi potential.
- 2) A finely subdivided, nonuniform mesh is utilized for improved accuracy of the numerical results.
- 3) Poisson’s equation is reduced to two first-order differential equations such that an exact Jacobian matrix can be formulated.
- 4) In order to insure robust large-signal time-dependent simulations, the right-hand side of equation (1) is discretized using a fully implicit (backward Euler) finite difference discretization scheme. For DC simulations, the right-hand side of this equation reduces to zero, emphasizing the required constancy of the electron particle current density.

Overall, the two equations obtained from Poisson’s equation, along with equations (1) and (2), yield the state variable set $J_{n,p}$, ϕ_n , ψ , and D . After “folding/

translating” of the device domain, twelve carrier transport equations must be solved at a given bias value subject to the heterointerface constraints and ideal ohmic contact boundary constraints. In order to derive an entire I-V curve or time-domain current waveform, as well as to obtain information about the internal physics of the device as a function of bias, the DC or AC bias is incrementally changed from the zero-bias condition. At each bias value, Newton iterations continue until the maximum change in the electrostatic and electron quasi-Fermi potentials across the entire mesh is less than $10^{-5} kT/q$ at 300 K. A typical bias-point solution is obtained, with this level of convergence and over a mesh containing 500 grid points, in 3 to 5 Newton iterations. On an HP Apollo 9000 Series 735 workstation, this corresponds to an average CPU execution time of approximately two seconds.

Finally, static C-V characteristics are obtained from the state variables by calculating the change in charge with respect to the change in applied DC bias over the depletion side of the device for sufficiently small increments in the device bias. Likewise, the displacement current is obtained from the state variables by calculating the change in the electric displacement with respect to the simulation time step. Multiple barriers are modelled in an ideal fashion by assuming that the terminal voltage is equally divided among the barriers. Therefore, in the simulator, only one barrier is simulated with an terminal voltage equal to the total terminal voltage divided by the number of barriers. For asymmetric HBVs, which can suffer from self-biasing, the full multiple barrier structure would have to be simulated to self-consistently account for this phenomenon.

III. Harmonic-Balance Nonlinear Circuit Analysis Technique

The harmonic-balance nonlinear circuit analysis technique employed in this work is an extension of the multiple-reflection algorithm[8]. The time-domain current through the device is calculated by the numerical device simulator, for one period, as described in the previous section. The harmonic components of the current are extracted from the time-domain current waveform using a discrete fourier transform. A fixed-point iterative expression, derived from the robust multiple-reflection algorithm, is then used to update the total voltage applied directly across the active region of the device in terms of the circuit

embedding impedances, the harmonic components of the current, and the harmonic components of the voltage from the previous iteration. This iterative process continues until the harmonic components of the voltage converge to their steady-state values.

The novelty in the harmonic-balance algorithm utilized here is that, in deriving the fixed-point iterative voltage update expression, we use *a priori* knowledge, from Kirchhoff's voltage law, that the nonlinear device impedance will equal the negative of the linear circuit impedance for each of the undriven harmonics in the steady state. This eliminates the computationally intensive and possibly unstable Runge-Kutta numerical time-integration necessary in the multiple-reflection algorithm, and automatically calculates complex under-relaxation parameters for each harmonic component of the fixed-point iterative voltage update equation. A Steffenson numerical acceleration scheme, adopted from the secant methods of numerical analysis[9], is also utilized to greatly increase the computational speed and convergence properties of the harmonic-balance nonlinear circuit analysis. Unlike Newton-type techniques, the difficult and time-consuming numerical calculations needed to assemble Jacobian matrices and to solve large linear systems of equations are avoided, while a convergence rate nearly equal to that of Newton-type methods is maintained.

IV. Results and Discussion

A. DC Results

In order to verify the accuracy of the DC and AC numerical device simulators, and to investigate the relevant material parameters for an InGaAs/AlGaAs heterointerface, single barrier n GaAs/undoped GaAs/undoped $\text{Al}_{0.7}\text{Ga}_{0.3}\text{As}$ and n GaAs/n $\text{In}_{0.0-0.2}\text{Ga}_{1.0-0.8}\text{As}$ /undoped $\text{In}_{0.2}\text{Ga}_{0.8}\text{As}$ /undoped $\text{Al}_{0.7}\text{Ga}_{0.3}\text{As}$ HBV structures have been grown by the Naval Research Laboratory (NRL) using Molecular Beam Epitaxy (MBE). The GaAs/ $\text{Al}_{0.7}\text{Ga}_{0.3}\text{As}$ HBV structure has been processed into mesa-isolated whisker-contacted HBV devices using a process successfully employed to fabricate Alloy Ramp diodes and Gunn diodes. The process involves an ohmic contact lift-off process to form the device anodes, a mesa-isolation etch to electrically isolate the individual mesa devices, and

a polyimide passivation layer to protect and further isolate the individual mesa devices.

Four-wire measurements of the I-V characteristics of several devices from two different wafers are shown in Figure 2 along with the simulated I-V curve. Excellent correlation between the DC numerical device simulator and the experimental I-V results for the GaAs/Al_{0.7}Ga_{0.3}As HBVs has been obtained as shown by this figure. The simulated device consisted of a 200 Å undoped ($\approx 1 \times 10^{16} \text{ cm}^{-3}$) Al_{0.7}Ga_{0.3}As barrier surrounded by two 50 Å undoped ($\approx 5 \times 10^{15} \text{ cm}^{-3}$) GaAs spacer layers and two n-type GaAs modulation layers. The asymmetry in the I-V characteristics was attributed to an asymmetry in the doping and thicknesses of the modulation layers, and was verified by Secondary Ion Mass Spectroscopy (SIMS). One modulation layer was determined to have a length of approximately 2000 Å and a doping of approximately $9.5 \times 10^{16} \text{ cm}^{-3}$, while the other modulation layer was approximately 1750 Å in length and was doped approximately $6.0 \times 10^{16} \text{ cm}^{-3}$. The alloy composition of the 200 Å undoped AlGaAs barrier was also verified by SIMS to be 70% aluminum.

Excellent correlation between the DC numerical device simulator and experimental DC I-V and static C-V data from the literature has also been obtained for single barrier GaAs/Al_{0.7}Ga_{0.3}As, GaAs/Al_{0.4}Ga_{0.6}As, GaAs/In_{0.2}Ga_{0.8}As/Al_{0.4}Ga_{0.6}As, and In_{0.53}Ga_{0.47}As/In_{0.52}Al_{0.48}As on InP HBVs.

B. Large-Signal Time-Dependent Results

Before examining results from the unified numerical device/harmonic-balance nonlinear circuit simulator, it is instructive to examine how two candidate HBVs respond to a pure sinusoidal large-signal voltage excitation, i.e. in the absence of harmonic voltages impressed by an external circuit. Figure 3 shows the time-domain current waveforms for two such simulated HBVs subject to a 100 GHz, 6.0 V sinusoidal excitation voltage. The HBVs are 8 μm diameter, four barrier structures with 200 Å undoped ($\approx 1 \times 10^{16} \text{ cm}^{-3}$) Al_{0.7}Ga_{0.3}As barriers. Each barrier is surrounded by 50 Å undoped ($\approx 5 \times 10^{15} \text{ cm}^{-3}$) spacer layers and 3500 Å doped ($6 \times 10^{16} \text{ cm}^{-3}$) modulation layers. The first structure had GaAs spacer and modulation layers, while the second structure had 3000 Å GaAs/500 Å

$\text{In}_{0.0-0.2}\text{Ga}_{1.0-0.8}\text{As}$ modulation layers and $\text{In}_{0.2}\text{Ga}_{0.8}\text{As}$ spacer layers.

As Figure 3 shows, the total current from the $\text{GaAs}/\text{In}_{0.0-0.2}\text{Ga}_{1.0-0.8}\text{As}/\text{Al}_{0.7}\text{Ga}_{0.3}\text{As}$ HBV is larger than that from the $\text{GaAs}/\text{Al}_{0.7}\text{Ga}_{0.3}\text{As}$ for the same applied voltage. Fourier analysis of the applied voltage waveform and the resulting current waveforms has been utilized to obtain information about the fundamental and harmonic frequency components of the voltage and current, as well as about the complex device impedance at the fundamental frequency. The impedance of the $8\ \mu\text{m}$ $\text{GaAs}/\text{Al}_{0.7}\text{Ga}_{0.3}\text{As}$ device is $Z(f_0=100\ \text{GHz}) = 14.503 - j115.61\ \Omega$; for the $8\ \mu\text{m}$ $\text{GaAs}/\text{In}_{0.0-0.2}\text{Ga}_{1.0-0.8}\text{As}/\text{Al}_{0.7}\text{Ga}_{0.3}\text{As}$ device, the impedance is $Z(f_0=100\ \text{GHz}) = 15.492 - j94.596\ \Omega$. In terms of the harmonic content of the output current waveforms, the even harmonic components are negligible when compared to the components of the fundamental and third harmonic frequencies, as expected. This is especially clear from Figure 3 where the current waveforms are triangular in shape and, thus, primarily composed of odd harmonics. For the $8\ \mu\text{m}$ $\text{GaAs}/\text{Al}_{0.7}\text{Ga}_{0.3}\text{As}$ device, the ratio of the current magnitude at $3f_0$ to that at f_0 is approximately 0.264; for the $8\ \mu\text{m}$ $\text{GaAs}/\text{In}_{0.0-0.2}\text{Ga}_{1.0-0.8}\text{As}/\text{Al}_{0.7}\text{Ga}_{0.3}\text{As}$ device, this ratio is approximately 0.337. More importantly, the current magnitude at $3f_0$ is 6.788 mA for the $\text{GaAs}/\text{Al}_{0.7}\text{Ga}_{0.3}\text{As}$ device and increases to 10.54 mA for the $\text{GaAs}/\text{In}_{0.0-0.2}\text{Ga}_{1.0-0.8}\text{As}/\text{Al}_{0.7}\text{Ga}_{0.3}\text{As}$ device, an increase of approximately 55 % in the third harmonic component of the current waveform. As will be seen conclusively in the next section, these results indicate that the $\text{GaAs}/\text{In}_{0.0-0.2}\text{Ga}_{1.0-0.8}\text{As}/\text{Al}_{0.7}\text{Ga}_{0.3}\text{As}$ HBV should provide improved tripler performance when compared to the performance of the $\text{GaAs}/\text{Al}_{0.7}\text{Ga}_{0.3}\text{As}$ HBV. This is primarily because the $\text{GaAs}/\text{In}_{0.0-0.2}\text{Ga}_{1.0-0.8}\text{As}/\text{Al}_{0.7}\text{Ga}_{0.3}\text{As}$ HBV structure can be pumped harder before avalanche breakdown limits its performance. In addition, the slightly higher circuit embedding impedances required for near optimum performance indicate that broadband device/circuit matching should be possible.

C. Harmonic-Balance Results

The unified numerical device/harmonic-balance nonlinear circuit simulator was first compared to harmonic-balance results obtained using our harmonic-balance algorithm

in conjunction with a simple analytical device model. The device model used curve fits to the device I-V and static C-V characteristics as obtained from the numerical device simulator under DC excitation. The time-dependent device current $i(t)$ is, thus,

$$i(t) = I_{DC}(v(t)) + C_{Static}(v(t)) \frac{dv}{dt} \quad (11)$$

where the first term is the device particle current and the second term is the device displacement current.

Figure 5 shows a comparison of the current and voltage waveforms obtained from the full unified numerical device/harmonic-balance nonlinear circuit simulator with those obtained from the analytical device/harmonic-balance nonlinear circuit simulator for an 8 μm diameter, single 200 Å barrier GaAs/Al_{0.7}Ga_{0.3}As HBV subject to a 100 GHz, 30 mW pump signal. The parameters for this device are the same as those of the four barrier GaAs/Al_{0.7}Ga_{0.3}As HBV previously outlined. For the harmonic-balance simulations, a device parasitic series resistance of 4.0 Ω was assumed, and fundamental and third harmonic circuit embedding impedances of $Z(f_1=100 \text{ GHz}) = 12.0 + j56.0 \Omega$ and $Z(f_3=300 \text{ GHz}) = 12.0 + j20.0 \Omega$, respectively, were used. All other embedding impedances were set to short circuit values of 0.001 + j0.000 Ω . Although the resulting current and voltage waveforms have the same general shape, the sharpness and magnitudes of the waveforms differ substantially. More importantly, the predicted absorbed power, third harmonic output power, and multiplying efficiency are substantially overestimated by the analytical device/harmonic-balance nonlinear circuit simulator. In particular, the analytical device/harmonic-balance nonlinear circuit simulator predicted an absorbed power of 7.87 mW and a third harmonic output power of 0.95 mW (multiplying efficiency of 12.07 %) as compared to an absorbed power of 10.40 mW and a third harmonic output power of 0.43 mW (multiplying efficiency of 4.17 %) for the full unified numerical device/harmonic-balance nonlinear circuit simulator.

From these results, it is clear that the time-dependent behavior of electrons in HBVs is not adequately accounted for using a simple analytical device model in conjunction with the harmonic-balance nonlinear circuit analysis. As a consequence, the results obtained

with such an analytical device model are significantly different from those obtained with a full numerical device model utilizing hydrodynamic transport equations where the dynamic high frequency nonstationary behavior of carriers is more accurately modeled.

Finally, it is instructive to compare the harmonic-balance results from the full numerical device/harmonic-balance nonlinear circuit simulator with the results obtained for HBVs subject only to large-signal time-dependent *sinusoidal* (fundamental) excitation. The HBVs analyzed are the 8 μm diameter, four barrier GaAs/Al_{0.7}Ga_{0.3}As and GaAs/In_{0.0-0.2}Ga_{1.0-0.8}As/Al_{0.7}Ga_{0.3}As HBV structures outlined in the previous section. Figure 6 shows the steady-state harmonic-balance current and voltage waveforms for the GaAs/Al_{0.7}Ga_{0.3}As HBV structure with a parasitic series resistance of 8.0 Ω and circuit embedding impedances of $Z(f_1=100 \text{ GHz}) = 23.0 + j115.6 \Omega$ and $Z(f_3=300 \text{ GHz}) = 23.0 + j75.0 \Omega$. Likewise, Figure 7 shows the steady-state harmonic-balance current and voltage waveforms for the GaAs/In_{0.0-0.2}Ga_{1.0-0.8}As/Al_{0.7}Ga_{0.3}As HBV structure with a parasitic series resistance of 8.0 Ω and circuit embedding impedances of $Z(f_1=100 \text{ GHz}) = 30.0 + j90.0 \Omega$ and $Z(f_3=300 \text{ GHz}) = 30.0 + j38.0 \Omega$. These circuit embedding impedances are believed to be fairly optimum values, although a complete optimization has not yet been completed.

For both HBV structures, the predicted absorbed power is $\approx 34.4 \text{ mW}$ for a pump power of 35.0 mW, and the predicted third harmonic output power is $\approx 2.4 \text{ mW}$ for a multiplying efficiency of $\approx 7.0 \%$. These values should improve with lower parasitic device series resistances. An important thing to note is that the real parts of the circuit embedding impedances are higher and, thus, easier to realize for the GaAs/In_{0.0-0.2}Ga_{1.0-0.8}As/Al_{0.7}Ga_{0.3}As HBV structure. This may be an important consideration in the design of broadband frequency multipliers using HBVs since good device/circuit matching is required over a broad frequency range. It is also important to note that the GaAs/Al_{0.7}Ga_{0.3}As HBV structure, under the given pumping conditions and with the fairly optimum circuit embedding impedances cited above, is being pumped at its maximum level when avalanche breakdown is considered. The GaAs/In_{0.0-0.2}Ga_{1.0-0.8}As/Al_{0.7}Ga_{0.3}As HBV structure, on the other hand, is being pumped at only about 69 % of its maximum

level under the given pumping conditions and with the fairly optimum circuit embedding impedances cited above. As a result, improved tripler performance is expected from a GaAs/In_{0.0-0.2}Ga_{1.0-0.8}As/Al_{0.7}Ga_{0.3}As HBV when compared to the performance of the GaAs/Al_{0.7}Ga_{0.3}As HBV.

V. Conclusions

In conclusion, an accurate and fast DC and large-signal time-dependent numerical device simulator for generic GaAs/InGaAs/AlGaAs and InGaAs/InAlAs on InP HBVs has been developed based on a physical model which combines current transport through the heterostructure bulk with current across the abrupt heterointerfaces in a fully self-consistent manner. The simulator can model any combination of doping and InGaAs, AlGaAs, or InAlAs alloy composition profiles, and provides an excellent tool for examining the DC and large-signal time-dependent characteristics of candidate HBV frequency multipliers. A novel and efficient harmonic-balance nonlinear circuit analysis technique has been developed which allows hydrodynamic-type device simulators to be used in place of typical analytical device or equivalent circuit models. The numerical device simulator has been successfully combined with the harmonic-balance nonlinear circuit simulator to provide a unified computer-aided design environment for the entire HBV multiplier circuit. HBV multiplier circuits can, therefore, be co-designed from both a device and a circuit point of view by specifying the device geometry, doping profile, and alloy composition profile, as well as the parasitic impedances of the device and the embedding impedances of the circuit.

Excellent correlation between the numerical device simulator and experimental DC I-V and static C-V data has been obtained for GaAs/AlGaAs, GaAs/InGaAs/AlGaAs, and InGaAs/InAlAs on InP HBVs. Large-signal time-dependent simulations of GaAs/Al_{0.7}Ga_{0.3}As and GaAs/In_{0.0-0.2}Ga_{1.0-0.8}As/Al_{0.7}Ga_{0.3}As HBVs under pure sinusoidal voltage excitation indicate that a significant improvement in the magnitude of the output current waveform can be obtained with the GaAs/In_{0.0-0.2}Ga_{1.0-0.8}As/Al_{0.7}Ga_{0.3}As HBV structure. More importantly, harmonic-balance nonlinear circuit simulations of these two

HBV structures indicate that third harmonic output power levels of several milliwatts and multiplying efficiencies of at least 7.0 % are obtainable with realizable fundamental and third harmonic circuit embedding impedances. The harmonic-balance simulations also show that the $\text{GaAs/In}_{0.0-0.2}\text{Ga}_{1.0-0.8}\text{As/Al}_{0.7}\text{Ga}_{0.3}\text{As}$ HBV structure can be pumped significantly harder than the $\text{GaAs/Al}_{0.7}\text{Ga}_{0.3}\text{As}$ HBV. Overall, the use of graded InGaAs/GaAs modulation layers should yield improved tripler performance when compared to a typical GaAs/AlGaAs HBV.

Acknowledgments

J. R. Jones is supported by a United States Air Force Laboratory Graduate Fellowship under the sponsorship of the Solid-State Directorate, Wright Laboratory, WPAFB, OH. This work is also partially supported by the NSF Grant #ECS-8720850. The authors are grateful to Scott Katzer of the Naval Research Laboratory for growing the HBV MBE structures. The authors would also like to thank M. F. Zybura and T. W. Crowe of the University of Virginia, and N. R. Erickson of the University of Massachusetts for numerous technical discussions relevant to this work. SIMS analysis was performed by Charles Evans & Associates, Redwood City, California.

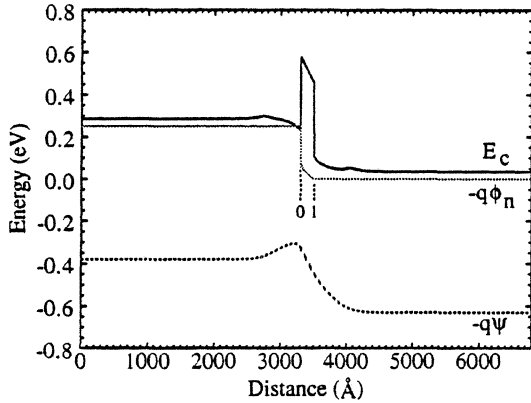


Figure 1. Band structure of n GaAs/n In_{0.0-0.2}GaAs/n In_{0.2}GaAs/n Al_{0.7}GaAs HBV biased at 0.25 V.

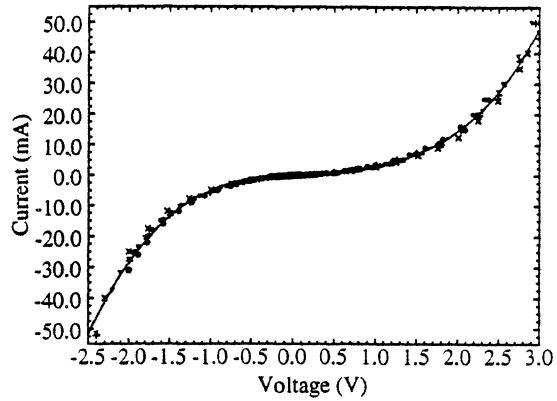


Figure 2. Experimental (symbols) and theoretical (solid line) I-V characteristics for 8 μm diameter mesa-isolated whisker-contacted n GaAs/n GaAs/n Al_{0.7}GaAs HBVs.

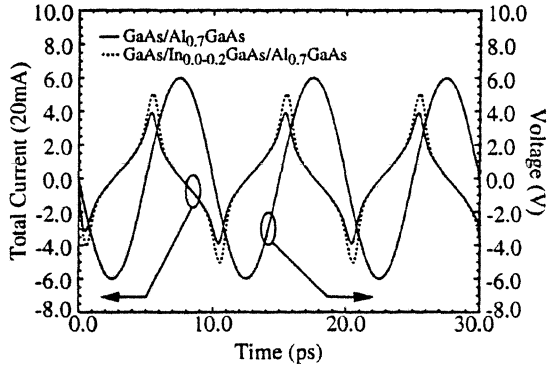


Figure 3. Current waveforms for 8 μm diameter, four 200 Å barrier $6 \times 10^{16} \text{ cm}^{-3}$ GaAs/Al_{0.7}GaAs and $6 \times 10^{16} \text{ cm}^{-3}$ GaAs/In_{0.0-0.2}GaAs/Al_{0.7}GaAs HBVs subject to 100 GHz, 6.0 V sinusoidal excitation.

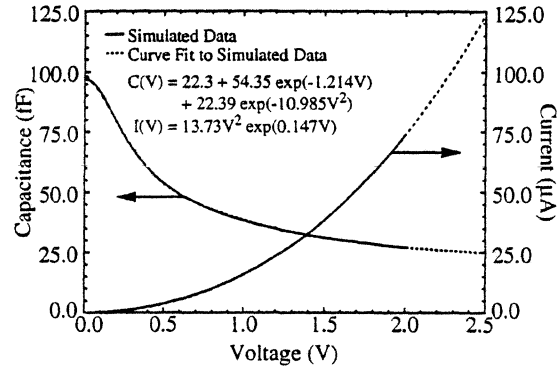


Figure 4. Simulated and curve-fit I(V) and C(V) characteristics for 8 μm diameter single 200 Å barrier $6 \times 10^{16} \text{ cm}^{-3}$ GaAs/Al_{0.7}GaAs HBVs.

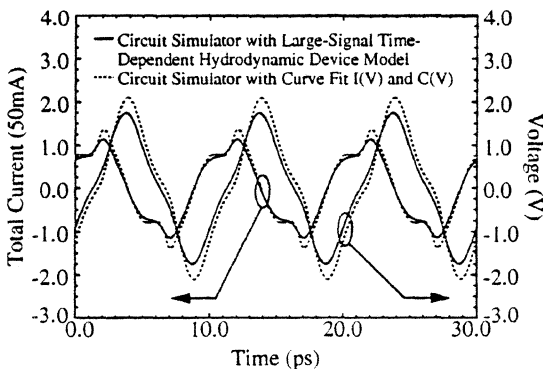


Figure 5. Steady-state harmonic-balance current and voltage waveforms for 8 μm diameter, single 200 Å barrier $6 \times 10^{16} \text{ cm}^{-3}$ GaAs/Al_{0.7}GaAs HBVs subject to 100 GHz, 30 mW excitation.

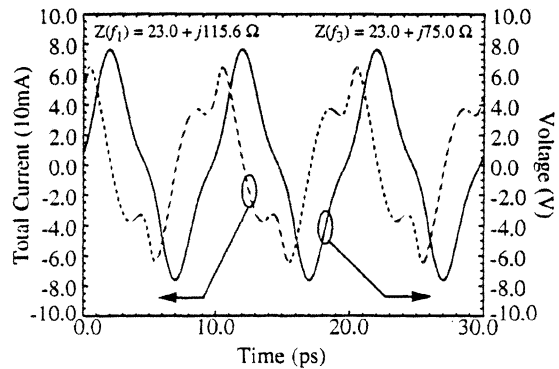


Figure 6. Steady-state harmonic-balance current and voltage waveforms for 8 μm diameter, four 200 Å barrier $6 \times 10^{16} \text{ cm}^{-3}$ GaAs/Al_{0.7}GaAs HBVs subject to 100 GHz, 30 mW excitation.

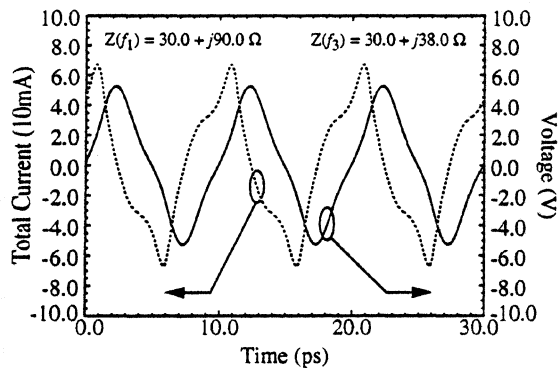


Figure 7. Steady-state harmonic-balance current and voltage waveforms for $8\ \mu\text{m}$ diameter, four $200\ \text{\AA}$ barrier $6 \times 10^{16}\ \text{cm}^{-3}$ GaAs/ $\text{In}_{0.0-0.2}\text{GaAs}/\text{Al}_{0.7}\text{GaAs}$ HBVs subject to 100 GHz, 30 mW excitation.

References

1. E. Kollberg and A. Rydberg, "Quantum-Barrier-Varactor Diodes for High-Efficiency Millimetre-Wave Multipliers," *Electron. Lett.*, Vol. 25, No. 25, Dec. 1989, pp. 1696-1698. Originally called the Quantum Barrier Varactor (QBV), we prefer to call the device the Heterostructure Barrier Varactor (HBV) to emphasize the importance of the heterostructure alloy composition and doping profiles in the design and operation of the device.
2. M. S. Lundstrom and R. J. Schuelke, "Numerical Analysis of Heterostructure Semiconductor Devices," *IEEE Trans. Electron Dev.*, Vol. ED-30, No. 9, Sept. 1983, pp. 1151-1159.
3. K. Horio and H. Yanai, "Numerical Modeling of Heterojunctions Including the Thermionic Emission Mechanism at the Heterojunction Interface," *IEEE Trans. Electron Dev.*, Vol. 37, No. 4, Apr. 1990, pp. 1093-1098.
4. G. B. Tait and C. R. Westgate, "Electron Transport in Rectifying Semiconductor Alloy Ramp Heterostructures," *IEEE Trans. Electron Dev.*, Vol. ED-38, No. 6, June 1991, pp. 1262-1270.
5. J. Adams and T. W. Tang, "A Revised Boundary Condition for the Numerical Analysis of Schottky Barrier Diodes," *IEEE Electron Dev. Lett.*, Vol. ED-7, No. 9, Sept. 1986, pp. 525-527.
6. E. H. Rhoderick and R. H. Williams, *Metal-Semiconductor Contacts*, 2nd Edition, Oxford, England: Clarendon, 1988, pp. 109-111.
7. G. B. Tait, "Heterostructure Semiconductor Device Analysis: A Globally Convergent Solution Method for the Nonlinear Poisson Equation," *Solid-State Electron.*, Vol. 32, No. 5, May 1989, pp. 369-376.
8. P. H. Siegel, A. R. Kerr, and W. Hwang, "Topics in the Optimization of Millimeter-wave Mixers," *NASA Tech. Papers*, No. 2287, Mar. 1984.
9. J. Ortega and W. Rheinboldt, *Iterative Solution of Nonlinear Equations in Several Variables*, New York, New York: Academic Press, 1970.